Universiteit Leiden
The Netherlands

Cathodic corrosion

Hersbach, T.J.P.

Citation
Hersbach, T. J. P. (2018, December 19). *Cathodic corrosion*. Retrieved from https://hdl.handle.net/1887/68033

Version:	Not Applicable (or Unknown)
License:	Licence agreement concerning inclusion of doctoral thesis in the Institutional Repository of the University of Leiden
Downloaded from:	https://hdl.handle.net/1887/68033

Note: To cite this publication please use the final published version (if applicable).

Cover Page

Universiteit Leiden

Leiden University Repository

The handle http://hdl.handle.net/1887/68033 holds various files of this Leiden University dissertation.

Author: Hersbach, T.J.P.
Title: Cathodic corrosion
Issue Date: 2018-12-19

3

Anisotropic Etching of Rhodium and Gold as the Onset of Nanoparticle Formation by Cathodic Corrosion

Cathodic corrosion alters metallic electrodes under cathodic polarization. Though these alterations can be dramatic, the exact mechanisms underlying cathodic corrosion are still unclear. This work aims to improve the understanding of cathodic corrosion by studying its onset on rhodium and gold electrodes in $10\ M$ *NaOH. The electrodes are studied before and after cathodic polarization, using cyclic voltammetry and scanning electron microscopy. This allows to define a corrosion onset potential of* $-1.3\ V$ *vs. NHE for rhodium and* $-1.6\ V$ *vs. NHE for gold. Furthermore, well-defined rectangular etch pits are observed on rhodium. Combined with rhodium cyclic voltammetry, this indicates a preference for forming (100) sites during corrosion. In contrast, a (111) preference is indicated on gold by voltammetry and the presence of well-oriented quasi-octahedral nanoparticles. We suggest this differing etching behavior to be caused by adsorption of sodium ions to surface defects, as is corroborated by density functional theory calculations.*

3.1 Introduction

All metals undergo oxidation under sufficiently anodic (positive) polarization, as can readily be deduced from the electrochemical series.[1] This oxidation lies at the basis of a variety of processes, such as formation of catalytically active metal oxides,[2] reorganization of the metallic surface[3] and corrosion and dissolution of material.[4] In contrast, metals are generally considered to be chemically stable under cathodic (negative) polarization; reduction of metals is not listed in the electrochemical series, Pourbaix diagrams generally consider uncharged metallic species to be most stable at low potentials,[5] and metals are commonly polarized cathodically to prevent anodic corrosion.[6]

This chapter is based on Hersbach, T. J. P., Mints, V. A., Calle-Vallejo, F., Yanson, A. I. & Koper, M. T. M., *Faraday Discussions* **193**, 207–222 (2016).

However, cathodic potentials are able to induce remarkable changes that are similar to those observed anodically, such as the generation of catalytically active undercoordinated sites[7] and reorganization of the surface.[8,9] In fact, it is even possible to degrade metallic electrodes in a process called cathodic corrosion.[10–12] This process etches metallic electrodes and is capable of forming nanoparticles by applying cathodic potentials, possibly by generating anionic metal intermediates. Though this process has typically been studied using strongly negative potentials,[13] Chapter 2 has demonstrated that the cathodic corrosion of platinum starts at the relatively mild potential of $-0.4\ V$ *versus* the reversible hydrogen electrode (RHE) in $10\ M$ NaOH. Furthermore, this chapter showed a strong preference for the creation of (100) sites during corrosion. In order to gain more insight into cathodic corrosion, it is important to explore the onset potential and etching preference of other metals. However, a key factor in determining these properties for platinum was the ability to create a reproducible electrode surface by flame annealing using a standard butane-oxygen burner,[14] which is not possible for all metals. Two of these metals are rhodium and gold: rhodium is rapidly covered by its oxide during annealing,[15] whereas gold electrodes of the required size melt almost immediately after reaching their glowing temperature.

In this study, we circumvent this problem by replacing the annealing step by a chemical cleaning step in which organic contaminants are removed from the electrodes using a 3:1 mixture of sulfuric acid and hydrogen peroxide. This procedure yields a highly polycrystalline, yet clean and reproducible electrochemical response for rhodium. A reproducible gold surface can also be created if repeated cyclic voltammograms (CVs) are performed in dilute sulfuric acid after chemical cleaning. After this preparation procedure, both rhodium and gold can be studied using the protocol from Chapter 2: electrodes are characterized using cyclic voltammetry in $0.1\ M$ H_2SO_4, after which they are treated cathodically in $10\ M$ NaOH. Subsequent cyclic voltammetry in H_2SO_4 will then reveal any changes in the electrode surface, allowing to pinpoint tentative cathodic corrosion onset potentials and detecting anisotropic etching preferences for both metals. Further study using scanning electron microscopy (SEM) reveals well-defined etch pits on rhodium and crystallites on gold, which are in excellent agreement with the electrochemically observed etching anisotropy. This etching anisotropy is explored further using density functional theory (DFT), which suggests the etching preference to arise from the specific adsorption of sodium ions to surface defects.

These results demonstrate that cathodic corrosion can occur as readily as anodic

corrosion, since both rhodium and gold etch anisotropically at mild cathodic potentials. Furthermore, this study provides a protocol for investigating cathodic corrosion on other metals that cannot be flame annealed, which is a crucial step in expanding cathodic corrosion studies.

3.2 Materials and methods

3.2.1 Electrochemistry

Electrochemical experiments were performed with an Autolab PGSTAT12. All water used in this study was demineralized and ultrafiltered by a Millipore MilliQ system (resistivity $> 18.2\ M\Omega \cdot cm, TOC < 5\ ppb$) before use. Working electrolytes were deoxygenated by purging argon (Linde, 6.0 purity) for at least 30 minutes prior to starting experiments. Deoxygenation was maintained by flowing argon over the solution during experiments.

Short lengths of Au (Materials Research Corporation, März Purity; $\varnothing = 0.125\ mm$) and Rh (Mateck, 99.9%; $\varnothing = 0.125\ mm$) wire were used as working electrodes. Each working electrode was rinsed with water, dipped in a 3:1 mixture of H_2SO_4 and H_2O_2 to remove organic contaminations and rinsed again before transfer into a standard 3-electrode cell filled with $0.1\ M$ H_2SO_4 (Merck, Ultrapur). This cell contained an Au or Pt spiral counter electrode for Au and Rh experiments, respectively. A reversible hydrogen electrode (RHE) was used as reference electrode and connected to an Au or Pt wire using a $4.7\ \mu F$ capacitor in order to filter noise during voltammetry. After careful immersion of the working electrode, which was controlled using a micrometer screw, gold electrodes were treated electrochemically by running 200 cyclic voltammetry cycles between 0 and 1.75 V *vs.* RHE at a scan rate of $1\ V \cdot s^{-1}$, in order to obtain a stable cyclic voltammogram (CV).[16] Such a cycling procedure was not necessary for rhodium. Next, the working electrodes were characterized by measuring four CVs at a scan rate of $50\ mV \cdot s^{-1}$.

Following characterization, the working electrodes were transferred to a home-made fluorinated ethylene propylene cell containing $10\ M$ NaOH (Fluka, Traceselect), a Ti counter electrode and a HydroFlex RHE (Gaskatel). After immersion of the working electrodes, a constant cathodic potential was applied for $60\ s$. This cathodic potential was not IR corrected, but ohmic drop estimates will be included in the text when relevant. Following polarization, working electrodes were removed from the electrolyte under potential control, rinsed and transferred back to the H_2SO_4 cell. In this cell, the electrodes were recharacterized using cyclic voltammetry. Finally, the working electrodes were taken out

of the cell, rinsed and stored for later analysis using scanning electron microscopy.

3.2.2 Scanning Electron Microscopy

Scanning electron micrographs were measured with a FEI NOVA NanoSEM 200 microscope, using an acceleration voltage of $5\ kV$ and a beam current of $0.9\ nA$.

3.2.3 Density Functional Theory

Density Functional Theory (DFT) calculations were performed using VASP,[17] the PBE exchange-correlation functional[18] and the projector augmented-wave (PAW) method.[19] The (111), (100), (211) and (553) surfaces contained four metal layers: the two topmost ones and the adsorbates were free to relax in all directions, while the two bottommost layers were fixed at the optimized bulk interatomic distances. The relaxations were performed with the conjugate-gradient scheme and a cut-off of $450\ eV$ for the plane-wave basis set, until the maximum force on any relaxed atom was below $0.01\ eV \cdot \text{Å}^{-1}$. $6 \times 6 \times 1$ k-point meshes were used for the 2×2 (111) surfaces; $6 \times 8 \times 1$ k-point meshes were used for the 3×2 (100) surfaces; $6 \times 4 \times 1$ k-point meshes were used for the 2-atom-wide (211) surface; and $5 \times 3 \times 1$ k-point meshes were used for the 2-atom-wide (553) surfaces. The distance between periodically repeated slabs was larger than 14 Å in all cases and dipole corrections were applied. For the calculations, $k_B T = 0.2\ eV$ was used, and the energies were extrapolated to $T = 0\ K$. Na was calculated in cubic boxes of 15 Å $\times$ 15 Å $\times$ 15 Å , using a gamma point distribution and an electronic temperature of $0.001\ eV$. The following reaction was used to assess the adsorption energies of Na:

$$^{*} + Na_{(g)} \rightarrow {}^{*}Na \tag{3.1}$$

where $*$ is a free adsorption site. Thus, the adsorption energies were calculated as:

$$\Delta E_{Na} = E_{*Na} - E_{*} - E_{Na} \tag{3.2}$$

3.3 Results and discussion

In an attempt to formulate coherent corrosion models for rhodium and gold, each metal will be discussed separately. First, we will discuss the electrochemical characterization of rhodium, which is followed by the corresponding scanning electron microscopy. These

observations will then be combined into a consistent corrosion model. Gold will be discussed in the same manner. Finally, we will draw parallels and highlight important differences between the corrosion characteristics of both materials, while also comparing them to the results for platinum from Chapter 2. The most notable difference, which is the different etching preference of these metals, will be explained with the aid of density functional theory calculations.

3.3.1 Rhodium

Electrochemical characterization

Rhodium electrodes were characterized using cyclic voltammetry. By measuring cyclic voltammograms in H_2SO_4 before and after the application of a constant cathodic potential in NaOH, we are able to detect changes in the electrode surface. Rhodium voltammograms feature two regions of particular interest. The first region lies above approximately 0.4 V *vs.* RHE and corresponds to the formation and reduction of surface rhodium oxide.[20] Though the shape of this region depends on the presence of various surface facets, the lack of sharp peaks impairs assessment of the relative distribution of surface sites.

This distribution can be assessed more reliably using the second CV region of interest, which lies below 0.3 V *vs.* RHE. Cathodic peaks in this region are attributed to a combination of hydrogen adsorption and (bi)sulfate desorption, whereas anodic peaks correspond to hydrogen desorption and (bi)sulfate adsorption. The location of these peaks relates directly to the distribution of surface sites. For this study, we will focus on the anodic peak, which is located respectively at 0.122 V, 0.157 V and 0.120 V *vs.* RHE for (111), (100) and (110) surfaces.[20]

Cyclic voltammograms of rhodium before and after cathodic polarization are displayed in Fig. 3.1. As can be seen in Panel **a**, several small changes are visible after cathodic polarization at −0.3 V *vs.* RHE. Firstly, a small shoulder develops on the anodic and cathodic peaks between 0.15 and 0.19 V *vs.* RHE. Secondly, the main cathodic and anodic peaks are slightly more well-defined after cathodic treatment. Though the exact reason for these changes is unclear, they appear consistently after polarization at and above −0.3 V *vs.* RHE. Finally, it is important to note that polarization at these potentials does not shift the location of the anodic peak by more than 1 mV (Fig. 3.2 **b**): it lies at approximately 0.121 V *vs.* RHE before and after treatment in NaOH. This position indicates a high abundance of (111) and (110) sites.

More prominent changes are visible after polarization at −0.4 V *vs.* RHE (Fig. 3.1 **b**):

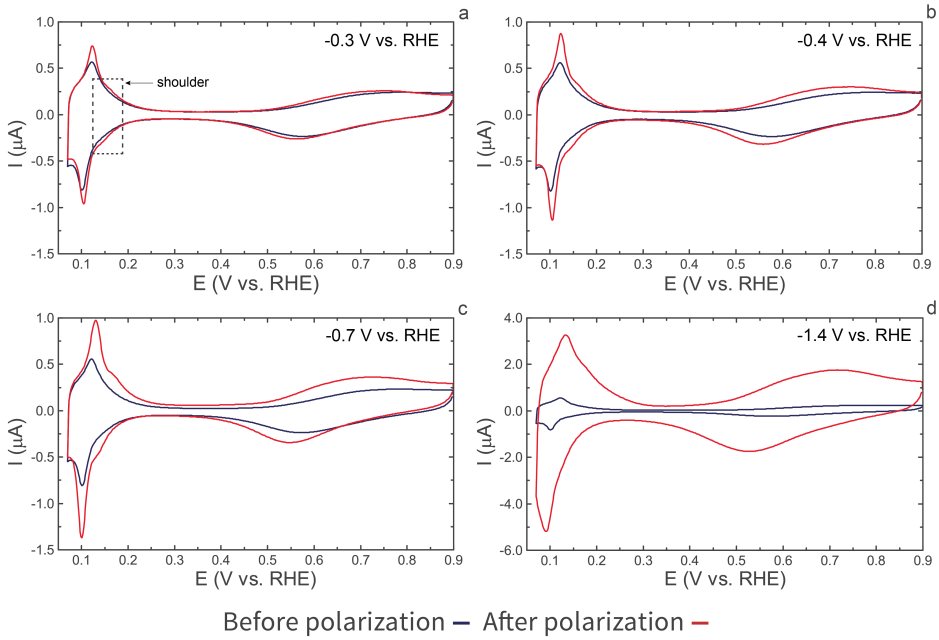

Fig. 3.1 | Cyclic voltammograms of rhodium electrodes before (blue trace) and after (red trace) cathodic polarization in 10 M NaOH at -0.3 V *vs.* RHE **(a)**, -0.4 V *vs.* RHE **(b)**, -0.7 V *vs.* RHE **(c)** and -1.4 V *vs.* RHE **(d)**. Voltammograms were recorded in 0.1 M H_2SO_4, at a scan rate of 50 $mV \cdot s^{-1}$.

the shoulder between 0.15 and 0.19 V *vs.* RHE is more pronounced and the charges corresponding to all oxidative and reductive surface reactions have increased. These changes, which become more prominent if the cathodic potential is lowered to -0.5 and -0.6 V *vs.* RHE, indicate an increase in the electrode area. This area increase is displayed as function of the polarization potential in Fig. 3.2 **a**. Furthermore, the hydrogen desorption peak shifts positively by approximately 2 mV. This shift increases slightly as the cathodic potential is decreased to -0.5 and -0.6 V *vs.* RHE (Fig. 3.2 **b**), which points towards a small increase in the relative abundance of (100) sites. Thus, cyclic voltammetry suggests that, after polarization at -0.4 V *vs.* RHE, the electrode is roughened by a process that favors the creation of (100) sites.

While the relative increase of (100) sites seems to develop only slightly until -0.6 V *vs.* RHE, a bigger increase in the amount of these sites is visible after treatment at -0.7 V *vs.* RHE (Fig. 3.1 **d**).* This is apparent from the position of the hydrogen desorption peak,

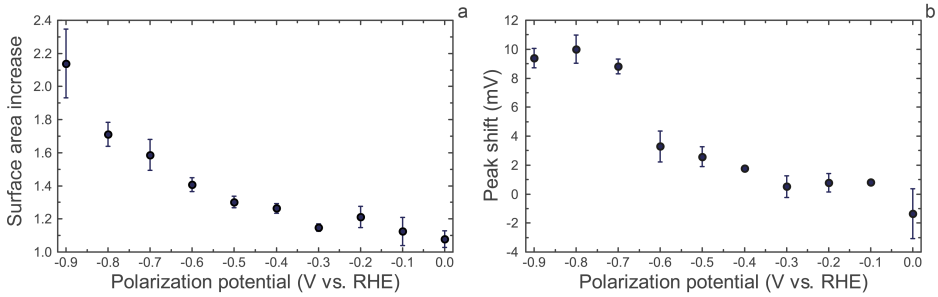

Fig. 3.2 | Relative rhodium surface area increase after cathodic polarization *vs.* polarization potential, as determined from the charge increase of the hydrogen desorption region **(a)**. Shift of the hydrogen desorption peak position after cathodic polarization *vs.* polarization potential **(b)**. Each data point is the average of 3 measurements and error bars represent one standard deviation. If no error bar is visible, it overlaps with its corresponding data point.

which shifts positively by roughly 9 mV, as is also visible in Fig. 3.2 **b**. This shift remains reasonably constant upon further lowering of the cathodic polarization potential. In contrast, the electrode area after polarization continues to increase monotonically (Fig. 3.2 **a**).

Though no other remarkable changes can be detected electrochemically, an important and surprising observation can be made visually: a black streak slowly extends from the electrode when a potential of -0.9 V *vs.* RHE[†] or lower is applied, which indicates detachment of nanoparticles from the electrode. This leads to severe roughening of the electrode, which is readily apparent from the voltammogram after treatment at -1.4 V *vs.* RHE:[‡] the increase in hydrogen desorption charge suggests that the electrode has 7.6 times more surface area, while the broadening of this peak is likely caused by the formation of nanoparticles.

[*] It should be noted that -0.7 V *vs.* RHE is the least negative applied potential for rhodium where ohmic drop effects start approaching the magnitude of the 0.1 V potential steps: an ohmic drop of approximately 0.05 V is present here.

[†] Ohmic drop causes the 'real' electrode potential to be -0.8 V *vs.* RHE.

[‡] Fully correcting for an estimated 240 mV ohmic drop and rounding to the nearest 100 mV leads to a 'real' electrode potential of -1.2 V *vs.* RHE.

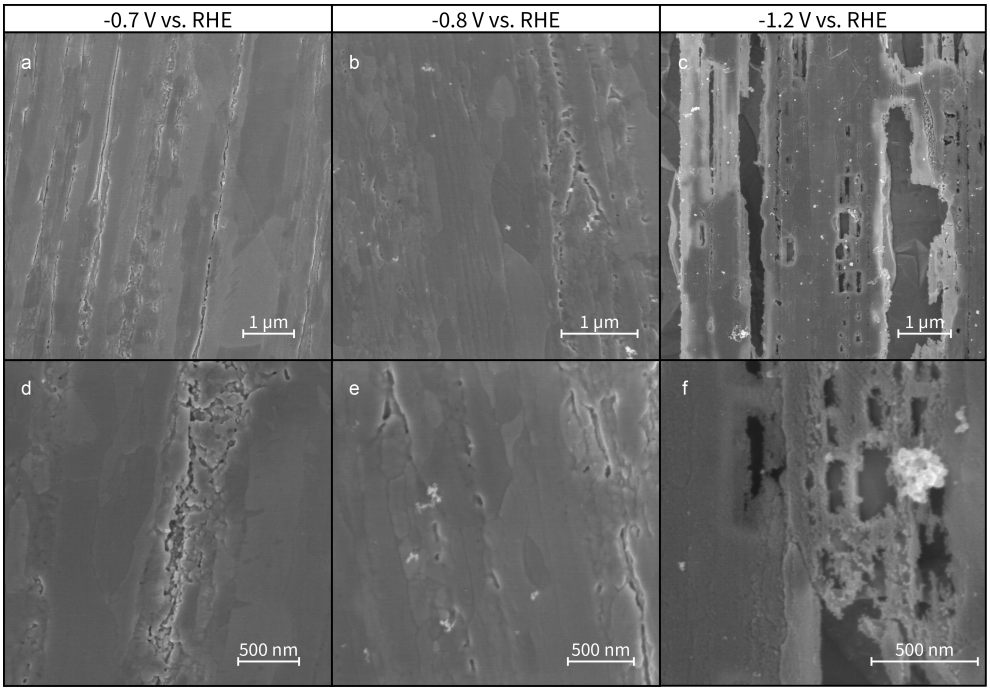

Fig. 3.3 | Scanning electron micrographs of rhodium electrodes treated at -0.7 *V vs.* RHE **(a**, **d)**, -0.8 *V vs.* RHE **(b**, **e)** and -1.2 *V vs.* RHE **(c**, **f)**.

Scanning electron microscopy

More information regarding the cathodic corrosion of rhodium can be gained by studying the polarized electrodes using scanning electron microscopy (SEM). Scanning electron micrographs of electrodes treated at -0.7, -0.8 and -1.2 *V vs.* RHE are presented in Fig. 3.3. These wire electrodes were mounted such that they are aligned vertically in the micrograph within a 5-degree error.

Several features stand out in micrographs of electrodes treated at or above -0.7 *V vs.* RHE (Fig. 3.3 **a**, **d**). Firstly, electrodes exhibit a high degree of polycrystallinity, since grain boundaries are visible at high magnifications. This polycrystallinity is also clearly visible in Fig. 3.3 as a variety of spots that appear to be darker than others, since grains with a significantly different orientation have a different contrast in SEM.[21,22] The degree of polycrystallinity is higher than that observed on platinum in Chapter 2, which is likely due to the platinum wires being flame-annealed before treatment. Such an annealing step should allow for merging of smaller grains. Secondly, electrodes typically exhibit

pits and ridges, such as those presented in Fig. 3.3 **d**. These ridges are not related to cathodic corrosion, because they are visible after polarization at all potentials above $-0.7\ V$ *vs.* RHE and on wires that were imaged without prior cathodic polarization. Thus, they are likely defects that were created during electrode preparation and not removed by an annealing step. Therefore, they do not seem to be related to cathodic corrosion, indicating that no signs of corrosion are detectable by SEM on wires that were treated at potentials of $-0.7\ V$ *vs.* RHE and higher.

In contrast, the effects of cathodic corrosion are ubiquitous on electrodes polarized at $-0.8\ V$ *vs.* RHE[§] or lower. As can be seen in Fig. 3.3 **b**, **e**, nanoparticle clusters of varying lengths are visible after cathodic treatment. These are the earliest sign of cathodic corrosion on rhodium. Upon decreasing the polarization potential to $-0.9\ V$ *vs.* RHE, rectangular etch pits such as those in Fig. 3.3 **c**, **f** start to develop. Though the borders of these pits are generally decorated with nanoparticles, their sides are offset by 90 degrees and the pit walls descend straight down. These etch pits can therefore be considered rectangles in terms of their outline and side-wall orientation, though their floor does not necessarily conform to this rectangular shape. Finally, it is interesting to note that these rectangles are always oriented such that their long sides are parallel to the wire direction.

Model

By combining the electrochemical and microscopic data, it is possible to formulate a preliminary model for the cathodic corrosion of rhodium. This process seems to start at approximately $-0.4\ V$ *vs.* RHE, since cyclic voltammetry indicates roughening of the electrode and the formation of (100) sites after polarization at this potential. However, more severe corrosion takes place below $-0.7\ V$ *vs.* RHE, as is indicated by a $9\ mV$ shift of the hydrogen desorption peak in voltammetry. Though any changes in the surface are too small to be detected by SEM after polarization at or above $-0.7\ V$ *vs.* RHE, nanoparticles can be seen after treatment at $-0.8\ V$ *vs.* RHE. These particles are accompanied by rectangular etch pits that are oriented along the wire if the potential is decreased to $-0.9\ V$ *vs.* RHE or lower. At this potential, dispersion of nanoparticles into the working solution is visible.

Though voltammetry before corrosion suggests that these etch pits are created in

[§] The electrode potential is $-0.7\ V$ *vs.* RHE after full ohmic drop correction.

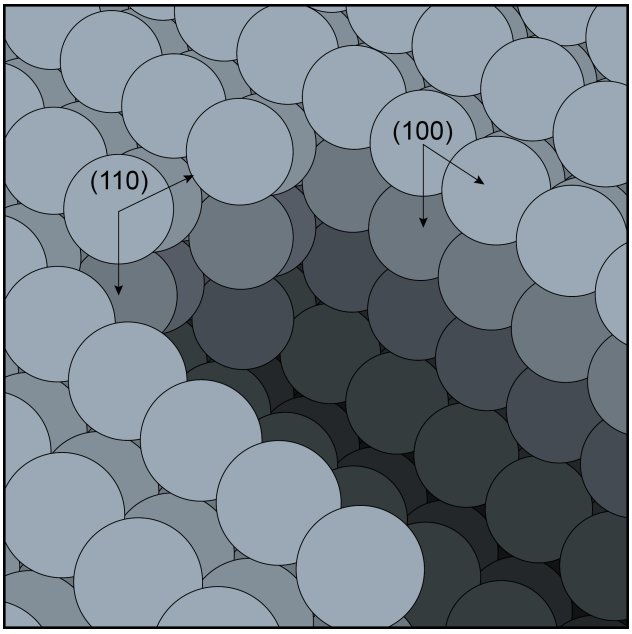

Fig. 3.4 | Model (110) surface with a rectangular etch pit. The bottom left and top right walls of the etch pit have a (100) orientation, whereas the top left side and bottom have a (110) configuration.

(111) or (110) surfaces, the shape of these pits rules out (111) surfaces; creating a (100)-type hole in a (111)-type surface will create triangular etch pits (Chapter 2). In contrast, creating a (100)-type hole in a (110)-type surface will form a rectangular hole with walls that are parallel to the [110] direction. These walls have a (100) surface orientation, as is visualized in the model etch pit in Fig. 3.4. Though the real cathodic corrosion etching kinetics are likely more complex than the formation of simple rectangles in an ideal (110) surface, the first-order approximation presented in Fig. 3.4 is able to explain important corrosion features by assuming the preferential formation of (100) sites in a (110)-type surface.

We will highlight two of these features. First of all, the model clarifies why the etch pits are rectangular and not square, since electrochemistry indicates that (100) sites are formed preferentially. Such preferential (100) site formation implies that the corresponding (100) pit walls should elongate at a higher rate than the (110) walls. This leads to the formation of a rectangular etch pit. Secondly, the model explains the orientation of the etch pits along the electrode direction, since it is likely that the grains in which they are formed are not oriented randomly due to the electrode production process.[23] Instead, it

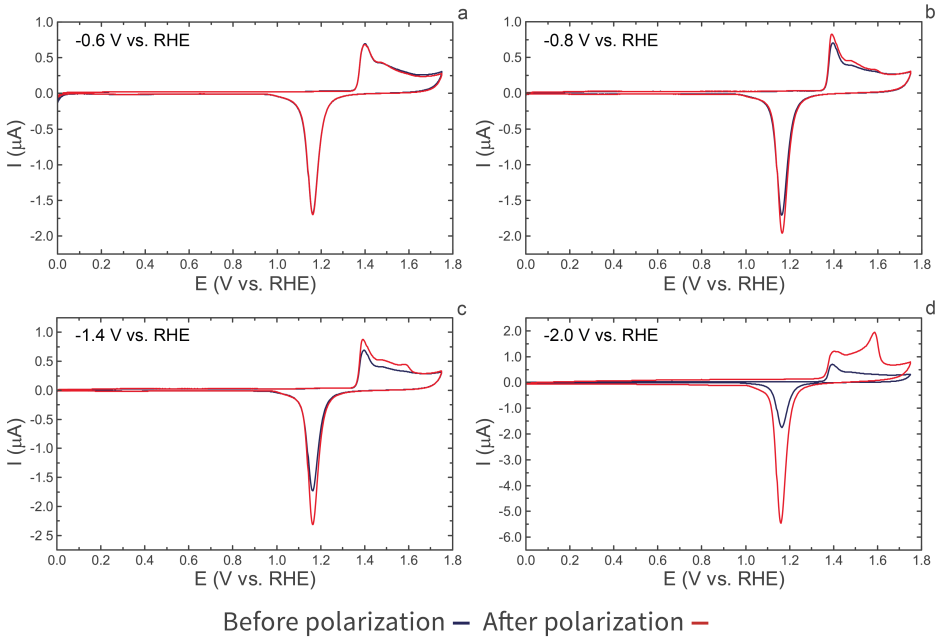

Fig. 3.5 | Cyclic voltammograms of gold electrodes before (blue trace) and after (red trace) cathodic polarization in 10 *M* NaOH at −0.6 *V vs.* RHE **(a)**, −0.8 *V vs.* RHE **(b)**, −1.4 *V vs.* RHE **(c)** and −2.0 *V vs.* RHE **(d)**. Voltammograms were recorded in 0.1 *M* H_2SO_4, at a scan rate of 50 $mV \cdot s^{-1}$.

is reasonable to assume that the [110] crystal axes are aligned with the wire direction: the voltammetry displayed in Fig. 3.1 suggests a (110) surface preference, while the shape of grains on non-corroded electrodes in Fig. 3.3 indicates a non-random grain orientation. Based on the surface mainly consisting of (110) grains with a fiber-like orientation along the wire, the model in Fig. 3.4 would then dictate that the etch pits should be aligned such that their long (100) walls lie along the wire direction.

3.3.2 Gold

Electrochemical characterization

In contrast with rhodium, gold does not exhibit any appreciable hydrogen adsorption in its voltammogram. Instead, its oxide formation region shows sensitivity towards the orientation of the surface.[24] CVs of gold electrodes before and after polarization at various potentials are shown in Fig. 3.5.

Fig. 3.5 **a** shows the typical behavior of gold electrodes when polarized at −0.6 *V vs.*

RHE or higher. No significant changes are induced by these cathodic potentials; the peak and shoulder in the voltammogram around 1.4 and $1.5\ V$ *vs.* RHE indicate that the electrodes exhibit features corresponding to (110) and (100) surfaces,[24] whereas a sharp feature corresponding to (111) sites around $1.59\ V$ *vs.* RHE is absent before and after cathodic treatment. In addition, the electrode surface area remains reasonably constant after cathodic polarization.

In contrast, a minor increase in surface area is indicated by a small increase in the charges associated with oxide formation and reduction after polarization at $-0.8\ V$ *vs.* RHE. However, this increase in area is not as reliable for defining the corrosion onset potential as it is for rhodium, since it is relatively small and is sometimes even observed for electrodes that were polarized above $-0.6\ V$ *vs.* RHE. A more reliable descriptor is the development of a distinct shoulder at $1.59\ V$ *vs.* RHE, corresponding to the formation of (111) sites. This development is subtle yet reproducible, so that closer inspection of the oxide formation region allows us to reveal the start of the formation of this (111) feature.

Such an analysis is performed in Fig. 3.6, which displays voltammograms of the oxide formation region of electrodes treated between -0.5 and $-0.8\ V$ *vs.* RHE. These voltammograms have been normalized by using the charge of the oxide reduction peak to determine the electrode surface area, assuming a specific charge of $390\ \mu A \cdot cm^{-2}$.[25] This normalization approach emphasizes relative changes in the orientation of the electrode surface. Fig. 3.6 does not show a (111) peak for electrodes treated at -0.5 and $-0.6\ V$ *vs.* RHE; both voltammograms run parallel at $1.59\ V$ *vs.* RHE. However, a (111) shoulder develops in this region after polarization at -0.7 and $-0.8\ V$ *vs.* RHE. This indicates an increase in the relative amount of (111) sites after treatment at these potentials.

The amount of (111) sites steadily increases upon lowering the cathodic treatment potential, as is visible in Fig. 3.5 **c**.[¶] Though the current in all regions of the oxide formation region has increased, the (111) peak at $1.59\ V$ *vs.* RHE is clearly visible. This peak continues developing as the treatment potential is lowered, which is visible in Fig. 3.5 **d**; a well-defined (111) peak is visible after corrosion and the increase in charge of the oxide reduction peak indicates a factor of 2.7 area increase.

[¶] For the gold experiments, the ohmic drop becomes significant at $-1.0\ V$ *vs.* RHE, where it shifts the potential by approximately $0.06\ V$. This causes the 'real' electrode potentials to be -1.2 and $-1.5\ V$ *vs.* RHE in Panel **c** and **d** of Fig. 3.5, respectively.

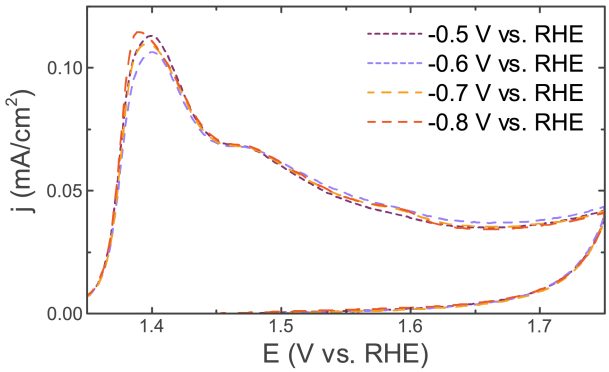

Fig. 3.6 | Voltammograms of the gold oxide formation region after polarization at $-0.5\ V$, $-0.6\ V$, $-0.7\ V$ and $-0.8\ V$ *vs.* RHE. Voltammograms were recorded in 0.1 M H_2SO_4, at a scan rate of 50 $mV \cdot s^{-1}$.

Scanning electron microscopy

Scanning electron microscopy (Fig. 3.7) allows for further analysis of the corrosion of gold. After polarization at $-0.9\ V$ *vs.* RHE or above (Fig. 3.7 **a**, **d**), the presence of many small crystal grains indicates a similar degree of polycrystallinity as rhodium. Another similarity with rhodium is the orientation of the grains, which show a fiber-like arrangement along the direction of the electrode. Finally, ridges are visible between some grain boundaries. As was the case for rhodium, the presence of these features can be attributed to the inability to flame anneal electrodes before experiments. No other remarkable features are present on the electrodes, indicating that no signs of corrosion are observable by SEM after polarization at and above $-0.9\ V$ *vs.* RHE.

When lowering the treatment potential to $-1.0\ V$ *vs.* RHE, no signs of corrosion can be seen at lower magnifications (Fig. 3.7 **b**). However, such signs are visible upon closer inspection of the crystal grains and ridges between them (Fig. 3.7 **e**). Along these ridges and on these grains, bright spots appear in the micrograph. These spots can be attributed to material budding out of the electrode. This budding becomes more pronounced as the cathodic potential is lowered. Furthermore, etch lines develop in the direction of the electrode, as is partly visible in Fig. 3.7 **c**. These lines indicate etching of gold, whereas the bright spots indicate redeposition of gold.

Along with etch lines, Fig. 3.7 **c** displays the formation of crystallites which are several hundreds of nanometers in size. These particles are first observable after polarization

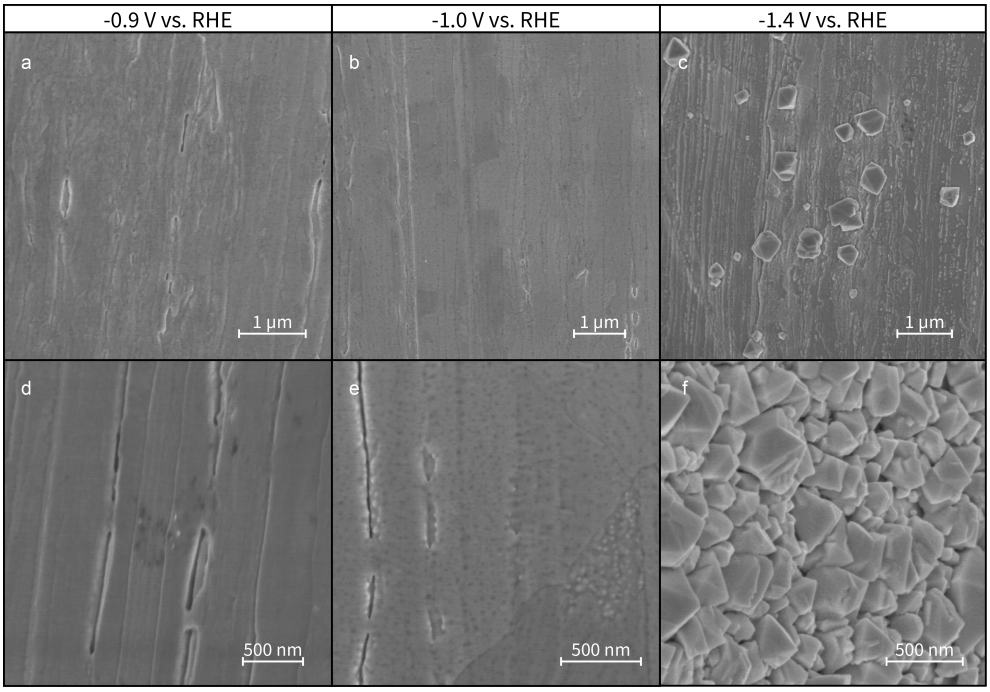

Fig. 3.7 | Scanning electron micrographs of gold electrodes treated at $-0.9\ V$ *vs.* RHE **(a**, **d)**, $-1.0\ V$ *vs.* RHE **(b**, **e)** and $-1.4\ V$ *vs.* RHE **(c**, **f)**.

at $-1.3\ V$ *vs.* RHE[‖] and predominantly contain 60° and 120° angles. The amount of observable particles increases as the cathodic potential is lowered. Their prevalence also increases towards the tip of the electrode, which is the furthest immersed point during polarization. This is readily visible when comparing Panel **c** and **f** in Fig. 3.7, since both micrographs were taken at different locations on the same electrode.

Model

These SEM and electrochemical observations lead to the following model of cathodic gold corrosion, which electrochemistry indicates to start at $-0.7\ V$ *vs.* RHE. This process favors the creation of (111) sites and initially leads to a minor increase in electrode surface area. Because this increase is small, no signs of corrosion are detectable by SEM until electrodes are polarized at or below $-1.0\ V$ *vs.* RHE. After polarization at these potentials, corrosion is initially visible as budding of material from the electrode surface.

‖ $-1.1\ V$ *vs.* RHE after 100% IR correction.

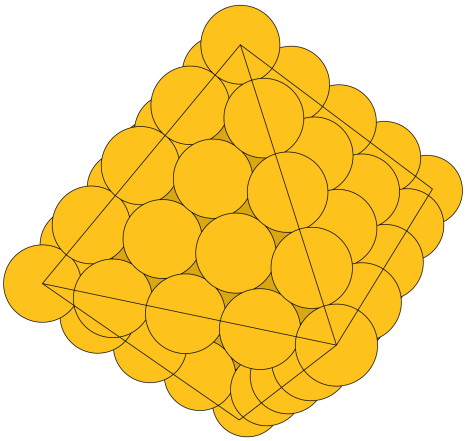

Fig. 3.8 | Model octahedral (111) nanoparticle.

Corrosion becomes more pronounced as the potential is lowered to -1.3 V *vs.* RHE, after which particles are visible.

The shape of these particles strongly suggests their surface to have the (111) orientation, as can be visualized using the model in Fig. 3.8. This model displays an octahedral gold nanoparticle, which exclusively exposes (111) surface sites. Though this is an ideal, high-symmetry model particle, it allows for the rationalization of the shape of the observed particles; the angles that should arise from the formation of (111) sites are immediately visible, since the model exclusively contains 60° angles. 120° angles can also be obtained, by simply merging two model particles through a shared surface. In fact, merging model particles of various sizes or selectively extending one of the sides of a model particle allows for a relatively satisfactory description of the particles in Fig. 3.7.

3.3.3 Comparison

After formulating models for the corrosion of rhodium and gold, comparing corrosion on these metals yields further insights.

Firstly, it is vital to notice the similar corrosion onset potentials for both rhodium and gold. Upon conversion to the normal hydrogen electrode (NHE) scale, these corrosion onset potentials respectively are -1.3 and -1.6 V *vs.* NHE for rhodium and gold, which is similar to the -1.3 V *vs.* NHE found for platinum in Chapter 2. Such potentials are relatively mild, especially in alkaline media; indeed, they are not too different from the potentials applied in reactions such as CO_2 reduction.[26] This supports the line of rea-

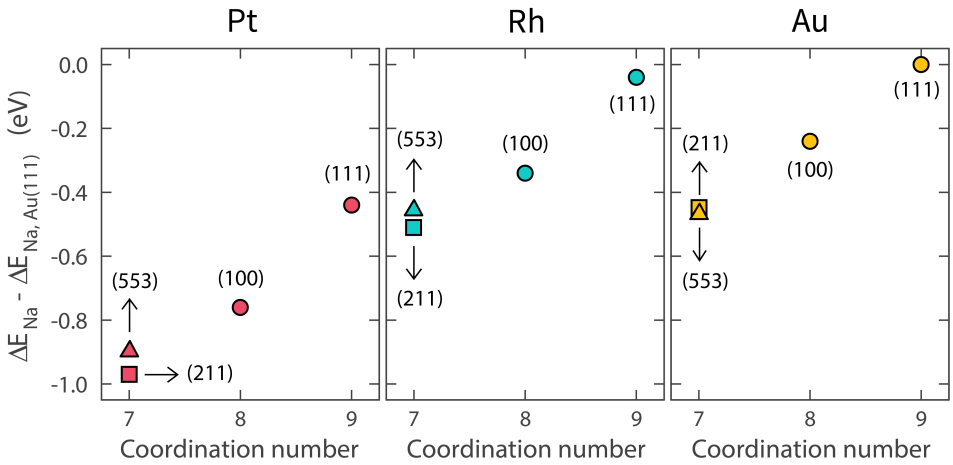

Fig. 3.9 | Adsorption energies of Na on various flat and stepped surfaces of Pt, Rh and Au, as a function of the coordination number of the adsorption sites. Energies are reported with respect to the adsorption of Na on Au(111).

soning that cathodic corrosion might, in fact, be just as detrimental to metal electrodes as the much better known phenomenon of anodic corrosion.

An important difference between both metals is their surface orientation preference. Gold favors the creation of (111) sites, whereas rhodium shows a preference for (100) sites. A similar (100) preference was observed for platinum in Chapter 2 and suggested to be caused by specific adsorption of sodium cations during cathodic polarization. This hypothesis is explored further in Fig. 3.9, which displays the DFT-calculated adsorption energy of sodium on the (111), (100), (211) and (553) facets of Rh, Pt and Au. The (211) and (553) surfaces both contain (111) terraces, but possess different step sites: (211) contains 3-atom-long (111) terraces and (100) steps (denoted [3(111)×(100)]), while (553) contains 5-atom-long (111) terraces and (111) steps (denoted [5(111)×(111)]). The adsorption on (211) and (533) surfaces was evaluated at these different steps. From Fig. 3.9, it is visible that sodium adsorbs strongest to platinum, followed respectively by rhodium and gold. This order is in agreement with the trends observed in scaling relations.[27,28] More importantly, Fig. 3.9 demonstrates that, for a given metal, sodium prefers to adsorb on open sites with lower coordination numbers; similar behavior has previously been observed for oxygen- and hydrogen-containing adsorbates.[29,30] Such an adsorption preference for steps indicates that adsorbate-induced anisotropies in cathodic corrosion should be caused by

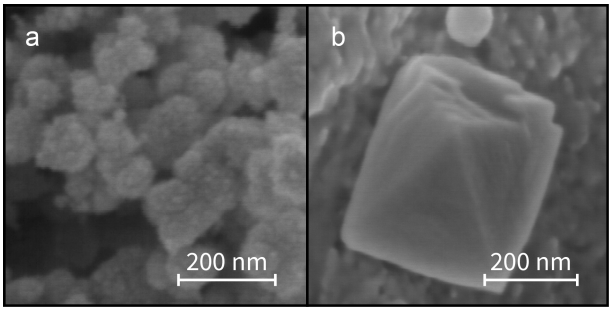

Fig. 3.10 | Scanning electrode micrographs of nanoparticles on a rhodium electrode treated at $-1.3\ V$ *vs.* RHE **(a)** and a gold electrode treated at $-1.4\ V$ *vs.* RHE **(b)**.

preferential sodium adsorption on steps or defect sites. Importantly, sodium adsorption is more favorable on (100)-type sites on rhodium and platinum, while it shows a small preference for (111)-type sites on gold. Thus, the DFT-calculated sodium adsorption energies are able to explain why platinum and rhodium preferentially expose (100) facets, while gold favors (111) facets: these sites are selectively stabilized by sodium adsorption. The minuteness of this stabilization on gold also indicates why the anisotropy at the onset of corrosion is less pronounced than for the other metals.

A second distinction between rhodium and gold is the size of their etch features and formed nanoparticles: a comparison of Fig. 3.3 & 3.7 demonstrates that rhodium displays much larger anisotropic etch features than gold, whereas the comparison of rhodium and gold nanoparticles in Fig. 3.10 demonstrates that gold forms larger anisotropic nanoparticles. This can tentatively be explained by the different mobility of surface atoms of the two metals. Since gold has a lower melting point and sublimation energy,[31] it is presumably more mobile than rhodium. This would allow gold to reconstruct more easily in order to minimize its surface energy, thereby counteracting the formation of etching features. In contrast, etching features in rhodium are lifted less easily by long-range reordering, causing the formation of large anisotropic etch pits. Similarly, the lower mobility of rhodium would lead to the formation of smaller nanoparticles with a high surface area such as those in Fig. 3.10 **a**, whereas gold particles can merge and reconstruct more easily to form larger particles with less exposed surface (Fig. 3.10 **b**). Thus, this difference in mobility does not only explain the differences observed in SEM, but also the electrochemically observed higher surface area increase for rhodium, as compared to gold.

3.4 Conclusions

In this work, we have studied the onset of cathodic corrosion on rhodium and gold. In doing so, we found tentative corrosion onset potentials of $-1.3\ V$ *vs.* NHE for rhodium and $-1.6\ V$ *vs.* NHE for gold in $10\ M$ NaOH. The mildness of these potentials suggests that cathodic corrosion can be at least as effective as anodic corrosion in inducing surface changes in metal electrodes.

Additionally, we were able to observe different crystallographic corrosion preferences for both metals: rhodium favors the formation of (100) sites, whereas gold preferentially forms (111) sites. This anisotropy is expressed in the formation of well-oriented rectangular etch pits on rhodium and quasi-octahedral nanoparticles on gold. The difference in anisotropy is attributed to the different adsorption of electrolyte cations on both metals, whereas the qualitative size differences in corrosion features are likely related to their different surface atom mobility.

Not only are these conclusions essential towards understanding cathodic corrosion, but the experimental procedure leading to these conclusions also provides a useful framework for studying cathodic corrosion on metals that cannot be flame-annealed.

3.5 Acknowledgements

We thank NCF with support from NWO for use of their supercomputers.

References

1. Vanýsek, P. in *CRC Handbook of Chemistry and Physics* (ed Haynes, W. M.) 96th ed., 5–80 – 5–89 (CRC Press, Boca Raton, FL, 2015).
2. Su, H.-Y. *et al.* Identifying active surface phases for metal oxide electrocatalysts: a study of manganese oxide bifunctional catalysts for oxygen reduction and water oxidation catalysis. *Physical Chemistry Chemical Physics* **14,** 14010 (2012).
3. Gómez-Marín, A. M. & Feliu, J. M. Pt(111) surface disorder kinetics in perchloric acid solutions and the influence of specific anion adsorption. *Electrochimica Acta* **82,** 558–569 (2012).
4. Cherevko, S. *et al.* Dissolution of Noble Metals during Oxygen Evolution in Acidic Media. *ChemCatChem* **6,** 2219–2223 (2014).
5. Pourbaix, M. *Atlas of electrochemical equilibria in aqueous solutions* 2nd ed., 644 (National Association of Corrosion Engineers, 1974).
6. V. Baeckmann, W., Schwenk, W. & Prinz, W. *Handbook of Cathodic Corrosion Protection* 3rd, 568 (Elsevier, 1997).
7. Declan Burke, L. & O'Mullane, A. P. Generation of active surface states of gold and the role of such states in electrocatalysis. *Journal of Solid State Electrochemistry* **4,** 285–297 (2000).

8. Kolb, D. Reconstruction phenomena at metal-electrolyte interfaces. *Progress in Surface Science* **51,** 109–173 (1996).
9. Kim, Y.-G., Baricuatro, J. H., Javier, A., Gregoire, J. M. & Soriaga, M. P. The Evolution of the Polycrystalline Copper Surface, First to Cu(111) and Then to Cu(100), at a Fixed CO2RR Potential: A Study by Operando EC-STM. *Langmuir* **30,** 15053–15056 (2014).
10. Haber, F. The Phenomenon of the Formation of Metallic Dust from Cathodes. *Transactions of the American Electrochemical Society* **2,** 189–196 (1902).
11. Kabanov, B. N., Astakhov, I. I. & Kiseleva, I. G. Formation of crystalline intermetallic compounds and solid solutions in electrochemical incorporation of metals into cathodes. *Electrochimica Acta* **24,** 167–171 (1979).
12. Yanson, A. I. *et al.* Cathodic Corrosion: A Quick, Clean, and Versatile Method for the Synthesis of Metallic Nanoparticles. *Angewandte Chemie International Edition* **50,** 6346–6350 (2011).
13. Yanson, Y. I. & Yanson, A. Cathodic corrosion. I. Mechanism of corrosion via formation of metal anions in aqueous medium. *Low Temperature Physics* **39,** 304–311 (2013).
14. Clavilier, J. & Chauvineau, J. P. Chemical characterization by Auger electron spectroscopy and voltammetry of platinum electrode surfaces prepared in the gas phase. *Journal of Electroanalytical Chemistry and Interfacial Electrochemistry* **100,** 461–472 (1979).
15. Carol, L. A. & Mann, G. S. High-temperature oxidation of rhodium. *Oxidation of Metals* **34,** 1–12 (1990).
16. Jeyabharathi, C., Ahrens, P., Hasse, U. & Scholz, F. Identification of low-index crystal planes of polycrystalline gold on the basis of electrochemical oxide layer formation. *Journal of Solid State Electrochemistry* **20,** 3025–3031 (2016).
17. Kresse, G. & Furthmüller, J. Efficient iterative schemes for ab initio total-energy calculations using a plane-wave basis set. *Physical Review B* **54,** 11169–11186 (1996).
18. Perdew, J. P., Burke, K. & Ernzerhof, M. Generalized Gradient Approximation Made Simple. *Physical Review Letters* **77,** 3865–3868 (1996).
19. Kresse, G. & Joubert, D. From ultrasoft pseudopotentials to the projector augmented-wave method. *Physical Review B* **59,** 1758–1775 (1999).
20. Xu, Q., Linke, U., Bujak, R. & Wandlowski, T. Preparation and electrochemical characterization of low-index rhodium single crystal electrodes in sulfuric acid. *Electrochimica Acta* **54,** 5509–5521 (2009).
21. Zauter, R. *et al.* Electron channelling contrast as a supplementary method for microstructural investigations in deformed metals. *Philosophical Magazine A* **66,** 425–436 (1992).
22. Canovic, S., Jonsson, T. & Halvarsson, M. Grain contrast imaging in FIB and SEM. *Journal of Physics: Conference Series* **126,** 012054 (2008).
23. Dillamore, I. L. & Roberts, W. T. Preferred Orientation in Wrought in Annealed Metals. *Metallurgical Reviews* **10,** 271–380 (1965).
24. Hamelin, A. Cyclic voltammetry at gold single-crystal surfaces. Part 1. Behaviour at low-index faces. *Journal of Electroanalytical Chemistry* **407,** 1–11 (1996).
25. Trasatti, S. & Petrii, O. Real surface area measurements in electrochemistry. *Pure and applied chemistry* **63,** 711–734 (1991).
26. Hori, Y. in *Modern Aspects of Electrochemistry* (eds Vayenas, C. G., White, R. E. & Gamboa-Aldeco, M. E.) 42nd ed., 89–189 (Springer New York, 2008).
27. Calle-Vallejo, F., Martínez, J. I., García-Lastra, J. M., Rossmeisl, J. & Koper, M. T. M. Physical and Chemical Nature of the Scaling Relations between Adsorption Energies of Atoms on Metal Surfaces. *Physical Review Letters* **108,** 116103 (2012).
28. Calle-Vallejo, F., Loffreda, D., Koper, M. T. M. & Sautet, P. Introducing structural sensitivity into adsorption–energy scaling relations by means of coordination numbers. *Nature Chemistry* **7,** 403–410 (2015).
29. Calle-Vallejo, F. *et al.* Finding optimal surface sites on heterogeneous catalysts by counting nearest neighbors. *Science* **350,** 185–189 (2015).

30. Tymoczko, J., Calle-Vallejo, F., Schuhmann, W. & Bandarenka, A. S. Making the hydrogen evolution reaction in polymer electrolyte membrane electrolysers even faster. *Nature Communications* **7,** 10990 (2016).
31. Haynes, W. M. *CRC Handbook of Chemistry and Physics* 96th ed. (ed Haynes, W. M.) 2677 (CRC Press, Boca Raton, FL, 2015).